MRS Communications (2018), *8*, 1236–1243
© Materials Research Society, 2018
doi:10.1557/mrc.2018.113

MRS Communications

Research Letter

Defect engineering in Boron Nitride for catalysis

Yi Ding, NanoScience Technology Center, University of Central Florida, 12424 Research Parkway, Orlando, FL 32826, USA; Department of Materials Science and Engineering, University of Central Florida, 12760 Pegasus Drive, Orlando, FL 32816, USA
Fernand Torres-Davila, NanoScience Technology Center, University of Central Florida, 12424 Research Parkway, Orlando, FL 32826, USA; Physics Department, University of Central Florida, 4111 Libra Drive, Orlando, FL 32816, USA
Ahmad Khater, NanoScience Technology Center, University of Central Florida, 12424 Research Parkway, Orlando, FL 32826, USA
David Nash, Physics Department, University of Central Florida, 4111 Libra Drive, Orlando, FL 32816, USA
Richard Blair, Florida Space Institute, University of Central Florida, 4111 Libra Drive, Orlando, FL 32816, USA
Laurene Tetard, NanoScience Technology Center, University of Central Florida, 12424 Research Parkway, Orlando, FL 32826, USA; Department of Materials Science and Engineering, University of Central Florida, 12760 Pegasus Drive, Orlando, FL 32816, USA; Physics Department, University of Central Florida, 4111 Libra Drive, Orlando, FL 32816, USA

Address all correspondence to Laurene Tetard at **Laurene.Tetard@ucf.edu**

(Received 29 March 2018; accepted 15 June 2018)

Abstract

Catalytic processes are critical steps in numerous industrial processes. The discovery of high reactivity of defects in metal-free two-dimensional materials has bolstered their emergence as catalysts. Here we consider the effect of defect-inducing methods in hexagonal boron nitride (*h*-BN) on their performance for olefin and CO_2 hydrogenation. We compare the changes introduced by ball milling and heat treatment in *h*-BN and show how varying the treatment conditions can impact the properties. We provide some evidence of the reactivity of the powders. Our results highlight how characterization can be exploited to assess the potential catalytic activity of *h*-BN for heterogeneous catalysis.

Introduction

Hexagonal boron nitride (*h*-BN) has long been used in applications requiring dry lubricants. In addition, its excellent electrical resistivity (with a dielectric strength of 80 $kV.mm^{-1}$), high thermal conductivity (71 $W.m^{-1}.K^{-1}$), and low thermal expansion ($<1 \times 10^{-6}$ K^{-1}) have made it a material of choice in industrial processes, such as for supports and cells used in chambers for high-temperature materials growth[1] or for large-scale exothermic reactions.[2] Remarkably, a recent body of work overhauls the conventional outlook on *h*-BN by suggesting that atomic arrangements in individual layers can be engineered to introduce a new generation of versatile catalysts.[3–7] This application has long been overlooked, partly due to the high chemical and thermal stability[1] together with the wide band gap of *h*-BN, estimated to be between 3.6[8] and 7.1 eV[9]. Instead, immediate applications of *h*-BN monolayers following the advent of two-dimensional (2D) materials such as graphene and transition metal dichalcogenides, have been in providing atomically thin and flexible insulating layers for nanoelectronics[10] and far-ultraviolet sources for optoelectronics.[11] At this time, all fields are converging toward the need for a deeper understanding of defects,[12–14] their formation and their effects on 2D materials properties, to reach more prevailing rules for material design in the foreseeable future.

Boron and nitrogen vacancies, together with Stone–Wales (SW) defects have been shown to be the most common defects found in individual *h*-BN layers,[3,15] beside edge defects. In multi-layered materials or heterostructures, stacking becomes another distinction that has to be taken into account.[16] All can significantly impact the optical,[17] electrical and magnetic properties of *h*-BN.[14] In addition, doping or impurities in place of the defects have led to interesting properties.[15] However, characterizing the nature of the defects remains challenging.[15] Secondary ion mass spectrometry can provide some insight on the carbon and oxygen content but the association with a particular defect is not straightforward.[15] Nanoscale imaging techniques including scanning probe microscopy and transmission electron microscopy (TEM) have revealed the presence of defects, in particular vacancies, but the effect of the incident beam such as in TEM could itself affect the nature of the defects. X-ray spectroscopies, electron energy loss spectroscopy, and electron-paramagnetic resonance[14] can also provide complementary information regarding the nature of the defects and the bond energies resulting from the presence of defects or impurities. However, this exercise remains challenging.

Hence, the effect of introducing defects in *h*-BN to create a new metal-free heterogeneous catalytic candidate taking the form of defect-laden hexagonal boron nitride (*dh*-BN), should be investigated further. It has now been confirmed that *dh*-BN can facilitate hydrogenation and olefin bond activation.[3,18] The experimental findings and conceptual predictions have been supplemented by density function theory (DFT)

https://doi.org/10.1557/mrc.2018.113 Published online by Cambridge University Press

calculations. The results show that the olefin bond will preferentially be activated over four types of defect sites in *h*-BN: boron substitution for nitrogen (B_N), nitrogen (V_N) or boron (V_B) vacancies, and SW defects.[3] Subsequent solid-state nuclear magnetic resonance (NMR) experiments identified nitrogen vacancies as the most probable active sites for olefin hydrogenation.[3]

Ball milling was the treatment used to produce dh-BN in the seminal study by Nash et al.[3] It is a common top-down approach to produce nanomaterials or to facilitate chemical reactions in the absence of solvents, potentially improving reaction efficiency.[19,20] This has been described for numerous applications including the realization of heterogeneous catalytic CO oxidation over metal oxide catalysts, such as NiO and Cr_2O_3,[19,21] and now for the hydrogenation and dehydrogenation on non-metal catalysts.[3] During ball milling, the flakes are mechanically exfoliated into thinner layers and reduced to smaller flakes through comminution, therefore increasing the surface area of the catalytic material.[3,22,23] Furthermore, it has been demonstrated that ball milling can introduce different types of defects, including edge defects and stacking disorder into *h*-BN flakes.[24,25] The nature and the density of defects may be controlled by varying operating parameters, i.e., milling intensity, duration and media composition. Nash et al.[3] further demonstrated that *dh*-BN produced through high energy ball milling can be utilized as a catalyst suitable for the hydrogenation of olefins in bulk-scale chemical experiments. Other processes of industrial relevance for producing defects, such as sintering or plasma etching, have not yet been carefully investigated for this application.

To date, the specific defects created and their role in the reactions have mostly been examined locally through gas chromatography—mass spectrometry analysis, solid-state NMR, and supported by quantitative measurements of binding energies such as with x-ray Photoelectron Spectra and DFT calculations.[3] For other 2D materials, Raman spectroscopy has been a powerful tool for identifying defects, particularly in graphene due to the disorder related D band.[26] In MoS_2, defects have been identified using the LA(M) band at ~227 cm^{-1}. LA(M) originates from the first-order Raman mode due to the LA phonons at the M point in the Brillouin zone.[27,28] The apparition of oxidation signs in the form of MoO_3 has also been used as an indicator of defect creation.[28]

In *h*-BN, identifying defect-induced properties is more challenging due to the absence of the D band indicative of defects present in graphene.[29] While scanning tunneling microscopy (STM) and TEM can offer high-resolution images of the atomic defects in 2D materials,[30,31] the requirement to deposit *h*-BN on a non-metallic substrate to study its metal-free catalytic properties makes it impractical for STM imaging. TEM is also challenging due to the thickness of the flakes in the powders used for ball-milling (sometimes greater than 50 layers). Thus, identifying defects in *dh*-BN to establish correlations with its catalytic properties continues to be quite challenging. However, comparing the effect of these defects on the reactivity of the formed *dh*-BN powders can provide valuable information for process optimization.

Motivated by the potential application of *h*-BN as a heterogeneous catalyst and the role defects play during the catalytic reactions, the present work investigates the effect of defects introduced in pristine *h*-BN through ball milling and heat treatment. A comparative study of the microstructure, physical and chemical properties of the *dh*-BN obtained under the various conditions is carried out to establish some connections with catalytic processes. Lastly, an initial assessment of the catalytic performance of the *dh*-BN powders is discussed.

Experimental methods

Sample preparation

Ball milling

The pristine *h*-BN powder was obtained from Saint-Gobain Ceramic Materials (Grade PCTF5). To remove moisture, the powder was dried at 180 °C in vacuum overnight before transferring to a glovebox filled with argon for ball milling. Two types of milling media and vials were used for milling, zirconia (ZrO_2, 12.7 mm in diameter, approximately 5.97 g in weight) and tungsten carbide (WC, 12.7 mm in diameter, approximately 16.5 g in weight). For each treatment, 3 g of dry *h*-BN powder were sealed in a 65 mL milling vial and four milling balls were employed to supply kinetic energy. After sealing the vial, the powder was processed with a mixer/mill (8000 M SPEX CertiPrep). When using the ZrO_2 balls, the powders were milled for 30, 60, 90, and 120 min. When using the WC balls, the powder was milled for 120 min. After milling, the *dh*-BN powder was stored in the glovebox until characterization. Upon transfer for spectroscopy measurements, the powder was sealed in a custom compartment to minimize exposure to air before characterization.

Heat treatment

Heat treatments were initially conducted in the air in a Thermolyne Small Benchtop Muffle Furnace (Type 1400, Thermo Scientific) for optimization. The parameters identified for defect creation were used to recreate the treatment in a controlled environment under glovebox conditions filled with argon. In both cases, pristine *h*-BN flakes from Saint-Gobain Ceramic Materials (Grade PCTF5) were transferred into the furnace, after the temperature was stabilized. At the end of the treatment, the samples were rapidly taken out from the furnace for fast cooling (or quenching) to room temperature. The detailed parameters used for heat treatment are listed in Table I.

Characterization

Scanning electron microscopy (SEM)

The morphology of *h*-BN and *dh*-BN powders, including shape and size, were studied using SEM (Zeiss ULTRA-55 FEG).

Raman spectroscopy

Raman spectra were acquired by using a confocal Raman microscope (WITec Alpha 300RA) with a 532 nm laser

https://doi.org/10.1557/mrc.2018.113 Published online by Cambridge University Press

Table I. Summary of the heat treatment conditions used for optimization of defect creation in pristine *h*-BN.

Heat treatment temperature (°C)	Duration (min)
800	120
850	120, 720 (12 h), 1440 (24 h)
900	120, 720 (12 h), 1440 (24 h)
950	120

excitation. Raman spectra were collected with a 50 × objective lens (Zeiss, numerical aperture of 0.7) and a spectrometer with an 1800 lines/mm grating, evaluated to provide a 0.9 cm^{-1} spectral resolution. For all spectra acquired, settings were maintained at a laser power of 5.7 mW and integration time of 1 s. Raman spectra from pristine *h*-BN powder and heat-treated *h*-BN powder prepared outside of the glovebox were acquired in air. Ball-milled and heat treated *dh*-BN powders prepared in the glovebox were sealed in custom-made chambers with a sapphire window (compatible for Raman measurements) inside the glovebox to prevent exposure to ambient conditions (H_2O, O_2, N_2, and CO_2).

Fourier transformed Infrared spectroscopy (FTIR)

FTIR spectra were acquired in the air, immediately after opening the sealed powder container, using a PerkinElmer FTIR spectrometer (Perkin Elmer Corp, Spectrum 100 series) equipped with an attenuated total reflection (ATR) sampling accessory unit with a single reflection diamond/ZnSe crystal plate. Because of the properties of the ATR windows, the wavelength range was restricted to 650–4000 cm^{-1}. The spectral resolution was set to 4 cm^{-1} with iris aperture of 8.9 mm for all measurements. Four scans were collected and averaged for each powder sample.

Results and discussion

We first investigated the effect of ball milling on the properties of *h*-BN. The morphology of the BN powders was studied using SEM to understand the effectiveness of ball milling in exfoliation and size reduction of the flakes. The morphology of the pristine *h*-BN flakes and the resulting *dh*-BN after ball milling are presented in Figs. 1(b) and 1(c–l), respectively. Higher resolution images are also provided in Fig. S1 (supplementary material). Analysis of the SEM images suggests that before treatment, the flakes were ~6–10 μm in size, in agreement with the product specification sheet (mean value of diameter: ~7 μm). The pristine flakes exhibited irregular edges but smooth surfaces and few folds or dislocations. After 30 min of milling with the ZrO_2 media, SEM images reveal flakes with smaller dimensions though large and intact flakes could still be observed [Figs. 1(c) and 1(d)]. This is attributed to the high-energy impact between the flakes, the milling balls and the vial walls during the treatment. As can be seen in

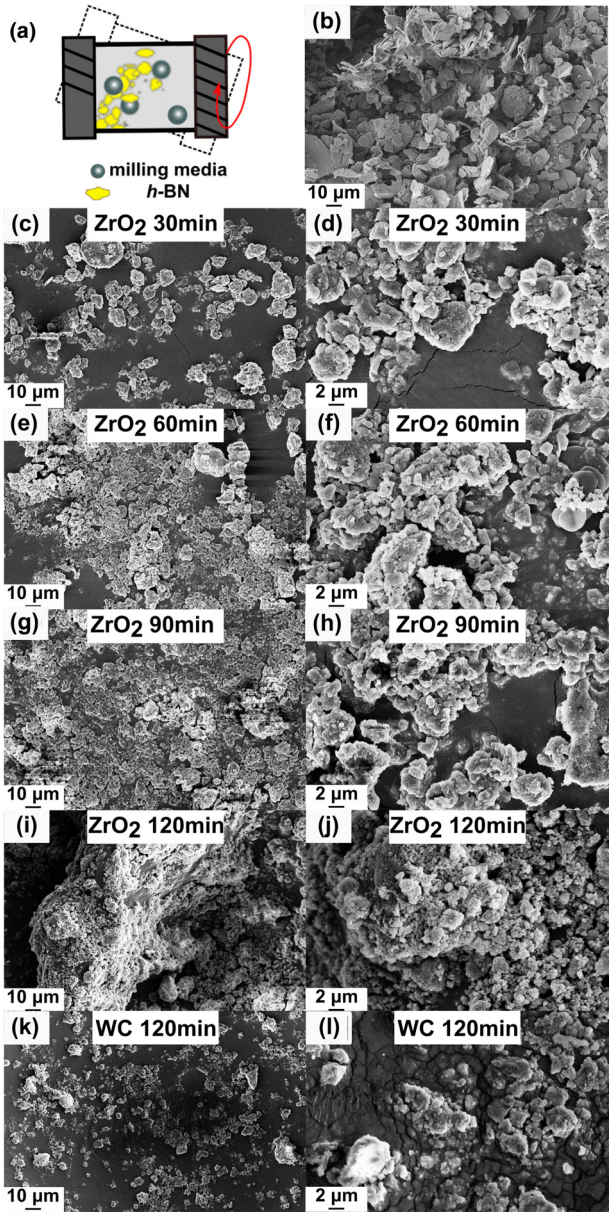


Figure 1. (a) Illustration of formation of dh-BN from pristine *h*-BN through ball milling, (b) SEM image of pristine *h*-BN flakes, (c–j) SEM image of *dh*-BN flakes after ball milling with ZrO_2 balls for 30 min (c and d), 60 min (e and f), 90 min (g and h), and 120 min (i and j). (k and l) SEM image of the *dh*-BN obtained after 120 min of treatment with WC milling balls. The SEM images presented in the right column correspond to a zoom of the images in the left column.

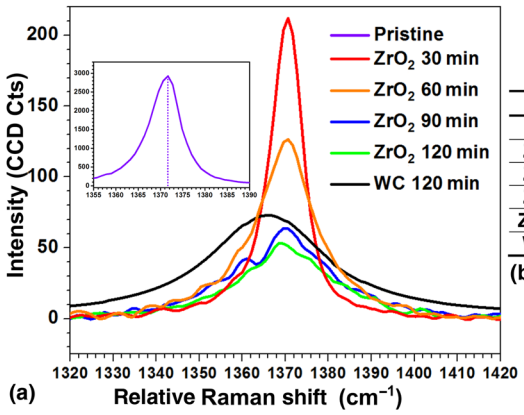
Table S1 (supplementary material), after the first 30 min, the large pristine flakes were mostly fragmented with flakes lateral dimensions in the 2–5 μm range. The number of 2–5 μm flakes increased until 60 min of treatment [Figs. 1(e) and 1(f)]. After 90 and 120 min, the dimension of the flakes decreased further, with a large number falling below 2 μm [Figs. 1(g)–(j)]. The SEM images also show that after 120 min of ball milling, the

https://doi.org/10.1557/mrc.2018.113 Published online by Cambridge University Press

lateral dimensions and thickness of the flakes decreased dramatically to nano-sized flakes and a significant agglomeration of the smaller flakes could be observed, which is in agreement with prior findings by Torii et al.[32] As a result, the percentage of edge defects in the volume of powder in the reactor increased for the first 120 min of milling with ZrO_2. Next, we considered the effect of the material of the milling media used on the process of defects generation by using WC milling balls for 120 min. The flakes obtained, as shown in Figs. 1(k) and 1(l), seemed to exhibit different morphology from those obtained at the same time point with ZrO_2. This was expected as the higher mass of the WC media should produce 2.76 times the impact force and kinetic energy compared with ZrO_2.

For all *dh*-BN powders considered in Fig. 1, the Raman and mid-infrared fingerprint of *h*-BN was affected by the introduction of defects. As both spectroscopies constitute direct measures of the molecular vibrations of chemical bonds in the material, the energy of the B-N lattice vibration may hold some information on the density and types of defects present in the flakes. Raman spectra of the *h*-BN and *dh*-BN powders collected for the different durations of milling are presented in Fig. 2. The positions and full width at half maximum (FWHM) of the BN mode at 1371 cm^{-1} were extracted using a Lorentz fit. A summary of the values is provided in Fig. 2(b). The band at 1371 cm^{-1} corresponds to the $E_{2\,g}$ phonon vibrational mode originating from the in-plane vibration of B and N atoms in opposite directions.[29] After the first 30 min of ball milling, a large decrease of the band intensity and broadening become apparent. Extended ball milling process intensified this effect. This can be attributed to the disorder introduced along the basal plane as the flakes get smaller. A slight red shift of the band from 1371 cm^{-1} for the pristine *h*-BN powder to 1370 cm^{-1} was observed within the first 30 min of ball milling. No further peak shift was measured despite the confinement of flake size as the milling duration increased from 30 to 120 min. Similar strain-induced red shifts of the analogous Raman G mode in graphene have previously been observed.[26,31] Based on these, we attribute the shift in *dh*-BN to the strain induced upon initial ball milling. FWHM exhibited a stronger dependence on milling duration as it increased gradually from 8.0 to 8.5 cm^{-1} after 30 min of treatment, and reached 24.5 cm^{-1} for 90 min of milling but remained constant for longer treatments. This significant increase in FWHM can be ascribed to a complex contribution from the increase in the strain or defect level inside the material and from the variation in surface scattering partly due to the distribution of *dh*-BN clusters with different dimensions and orientations, compared with the pristine *h*-BN flakes.[13] When milling the *h*-BN flakes with WC milling balls for 120 min, the $E_{2\,g}$ band shifted of about 6 cm^{-1} from 1371 cm^{-1} (pristine *h*-BN in purple in Fig. 2) to 1365 cm^{-1} (black in Fig. 2). In addition, a large broadening of the band to ~32 cm^{-1} was measured. The increase in the impact force and kinetic energy resulting from the higher mass of WC compared with ZrO_2 can explain this effect. These higher forces were found to result in more in-plane disorder.

Next, we compared the IR fingerprint of the *h*-BN powders obtained with FTIR spectroscopy (Fig. 3). *h*-BN exhibits two primary bands around 763 and 1358 cm^{-1}. The vibrational mode near 763 cm^{-1} corresponds to A_{2u} out-of-plane bending vibration of B-N-B, while the peak near 1358 cm^{-1} represents the E_{1u} in-plane stretching vibration of the B-N bond.[33,34] In addition, we note that for pristine *h*-BN powder, small bands around 2342 and 2542 cm^{-1} are present. They have previously been attributed to small molecules and impurities adsorbed on the pristine *h*-BN in air.[35,36] The first 30 min of ball milling seemed to remove contamination as the bands above 2000 cm^{-1} disappeared and the E_{1u} in-plane stretching band became narrower. Another weak band about 925 cm^{-1}, previously reported[37] as a B-O or B-N-O stretching mode in pristine BN,[37,38] disappeared after 30 min of ball milling. This indicates that some oxidation of *h*-BN or oxygen adsorption may take place in storage,



Sample	Position (cm^{-1})	FWHM (cm^{-1})
Pristine	1371	8.0
ZrO_2 30 min	1370	8.5
ZrO_2 60 min	1370	16.6
ZrO_2 90 min	1370	24.6
ZrO_2 120 min	1370	24.5
WC 120 min	1365	32.4

(b)

Figure 2. (a) Raman spectra exhibiting the $E_{2\,g}$ band ~1370 cm^{-1} of pristine *h*-BN (purple in inset) and *dh*-BN after ball milling with ZrO_2 for 30 min (red), 60 min (orange), 90 min (blue), 120 min (green), and with WC for 120 min (black). (b) Table summarizing the position and FWHM of the $E_{2\,g}$ band in ball-milled *h*-BN obtained with different durations of treatments with ZrO_2 and WC milling balls.

https://doi.org/10.1557/mrc.2018.113 Published online by Cambridge University Press

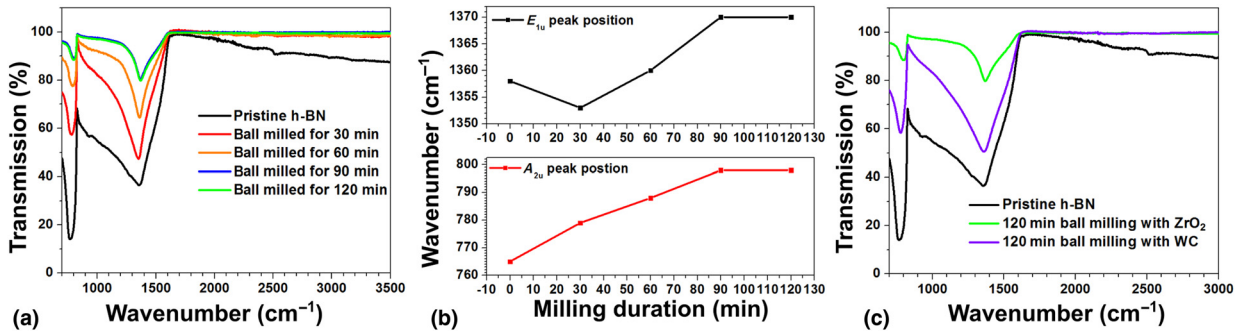


Figure 3. (a) FTIR spectra of *h*-BN and *dh*-BN obtained for milling times of 30 min, 60 min, 90 min, and 120 min with ZrO_2. (b) Evolution of E_{1u} (top, black) and A_{2u} (bottom, red) IR bands as a function of milling duration. (c) FTIR spectra of *h*-BN and *dh*-BN obtained after ball milling for 120 min with ZrO_2 (green) and WC (purple) milling balls.

but can be reversed by ball milling. This is in agreement with the induction period, i.e., the time required for *h*-BN to be processed in the ball milling reactor before any catalytic activity can take place, which has been observed in our measurements.

After increasing ball milling treatment durations, the respective intensities of the two *h*-BN characteristic bands were found to decrease. The quantity of powder and the force applied on the ATR crystal were maintained constant for all measurements. Hence, the reduction in the size of the BN flakes, leading to smaller crystalline regions to absorb the light, is likely responsible for the smaller band intensity. Another interesting point is that the ratio of Absorption$_{(A2u)}$/Absorption$_{(E1u)}$ was above 1(1.36) for pristine *h*-BN but continuously decreased from 0.81 at 30 min ball milling to 0.55 as 90 and 120 min (Table S2 in the supplementary material). This may suggest that the out-of-plane bending vibrations decreased as the exfoliation of the flakes progressed. However, the ratio observed for the powder obtained with WC balls was higher than for the powders obtained with the ZrO_2 balls. This remains unexplained at this time and should be investigated further. Next, we considered the position of the two bands. As shown in Fig. 3(b), the two bands shifted to higher wavenumber with increasing milling duration. For the A_{2u} peak, the position moved from 765 cm^{-1} for pristine *h*-BN to 779 cm^{-1} after 30 min milling before reaching a maximum at 798 cm^{-1} after 90 min milling. Similarly, the position of the E_{1u} band shifted from 1358 to 1370 cm^{-1} as the milling time increased from 0 to 90 min. No additional changes were found between 90 and 120 min. This is likely due to the change in strain the flakes as a result of exfoliation. Lastly, we compared the effect of milling with ZrO_2 or WC balls on the IR fingerprint of *dh*-BN powder obtained after 120 min [Fig. 3(c)]. We found that the position of the A_{2u} and E_{1u} bands did not significantly change given the 4 cm^{-1} resolution of the FTIR system. The results suggest that after 120 min, milling may have achieved its highest potential for defect creation in the volume of *h*-BN used when milling with ZrO_2 media. This is in agreement with a previous study by Torii et al.[32] in which the surface area available was found to decrease after a threshold of treatment duration, as an aggregation of the small flakes became predominant.

The effect of heat treatment on h-BN was investigated next. As shown in Fig. 4, no Raman shift or FWHM broadening was

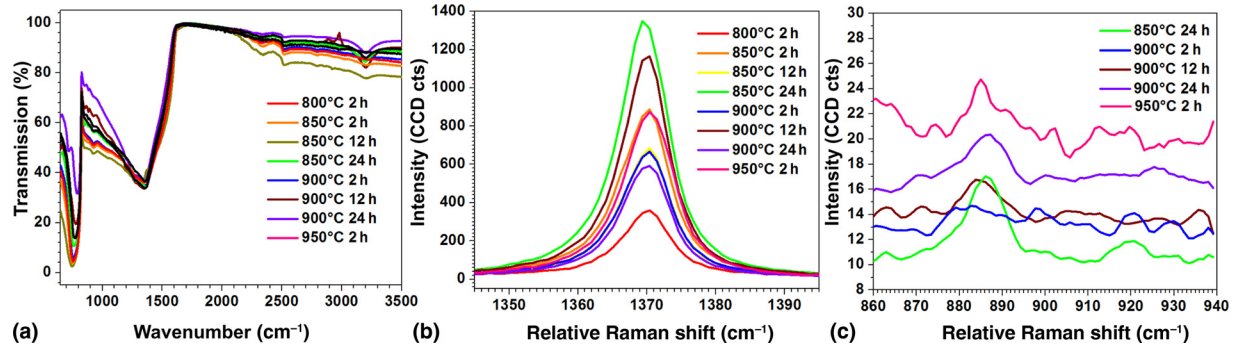


Figure 4. Effect of heat treatment on *h*-BN powders (a) FTIR spectra of BN powders heat treated at different conditions: 800 °C for 2 h (red), 850 °C for 2 h (orange), 850 °C for 12 h (green), 850 ° for 24 h (light green), 900 ° for 2 h (blue), 900 ° for 12 h (brown), 900 ° for 24 h (purple), 950 ° for 2 h (pink), (b) Corresponding Raman spectra representing the E_{2g} mode Raman peak of the heat treated BN powders (c) Raman band corresponding to the B-O bond for oxidized BN powder around 885 cm^{-1}.

https://doi.org/10.1557/mrc.2018.113 Published online by Cambridge University Press

observed following the treatment in the optimization phase, carried out in the air (Fig. 4 and Table S3 in the supplementary material). This is in agreement with a study by Li et al.[39] that found the Raman E_{2g} band unchanged by heat treatment of bulk *h*-BN. Based on our SEM images, we could estimate the flakes in the powder to be more than 50 layers thick. However, for powders heat treated with 850 °C for 24 h, 900 °C for 12 and 24 h, and 950 °C for 2 h, a Raman band centered near 886 cm^{-1} was observed, corresponding to the breathing mode of oxygens within a boroxol ring according to previous reports.[40,41] These observations and various DFT reports in the literature[3,14] allow us to infer that the creation of defects, most likely V_N, led to local *h*-BN oxidization into B_2O_3 as a result of the treatment under ambient conditions. After reproducing the measurements in the conditions of defect creation (950 °C for 2 h) but under the argon filled atmosphere, the Raman signature of the heat treated powder was obtained and indicated no sign of oxidation in the 800–900 cm^{-1} (Fig. S2). The FTIR signatures of the treated *h*-BN flakes exhibited the two bands at around 770 and 1360 cm^{-1} respectively, indicating that the crystal structure remains after heat treatment. This is also confirmed by the SEM image (Fig. S1). A strong (B-) O—H stretching IR peak near 3200 cm^{-1}[40] appeared for heat treated BN powder beyond 12 h (850 °C for 12 h, 850 °C for 24 h, 900 °C for 12 h, and 900 °C for 24 h). The powder treated at 900 and 950 °C for 2 h exhibited no detectable IR signals from (B-) O—H about 3200 cm^{-1}. However small bands at ~925 cm^{-1} and between 2000 and 3000 cm^{-1} previously associated with impurities in the powder,[37,38] which could be removed with short ball milling, remained on the flake for all heat treated powders. This could impede the reactivity of the flakes given our prior observations of a required induction period to remove impurities in ball milling before reactions can take place in the ball milling reactor.

These results indicate that both treatments affect the vibrational modes of the *h*-BN lattice with signs of defect formation. This is only meaningful if *dh*-BN exhibit catalytic properties for targeted reactions. To test this, we pressurized a representative powder of each treatment, the powder ball-milled with ZrO_2 for 2 h and the powder heat-treated at 950 °C for 2 h, with molecules of interest. We evaluated the reaction with olefin by pressurizing the cell at 40 PSI with propene for 48 h. For the reaction with CO_2, we pressurized the cell at 40 PSI with CO_2 for 48 h. The largest mass uptake, an about 6.8% increase, was observed for the ball-milled powder exposed to propene. The corresponding exposure with heat treated powder only saw a 0.2% uptake. After exposure to CO_2, a smaller mass uptake of 3% was found for the ball-milled powder while a 0.4% uptake was measured for the heat treated powder. The nature of the uptake on the ball-milled flakes was confirmed with FTIR spectroscopy (Fig. 5). The presence of two bands at ~2550 cm^{-1} (B-H stretching) and ~3400 cm^{-1} (region for O-H stretch in alcohol R_2CH_2OH or in carboxylic acid R_2COOH) in the CO_2-pressurized dh-BN powder [inset in Fig. 5(a)] suggests that the new bands corresponds to the

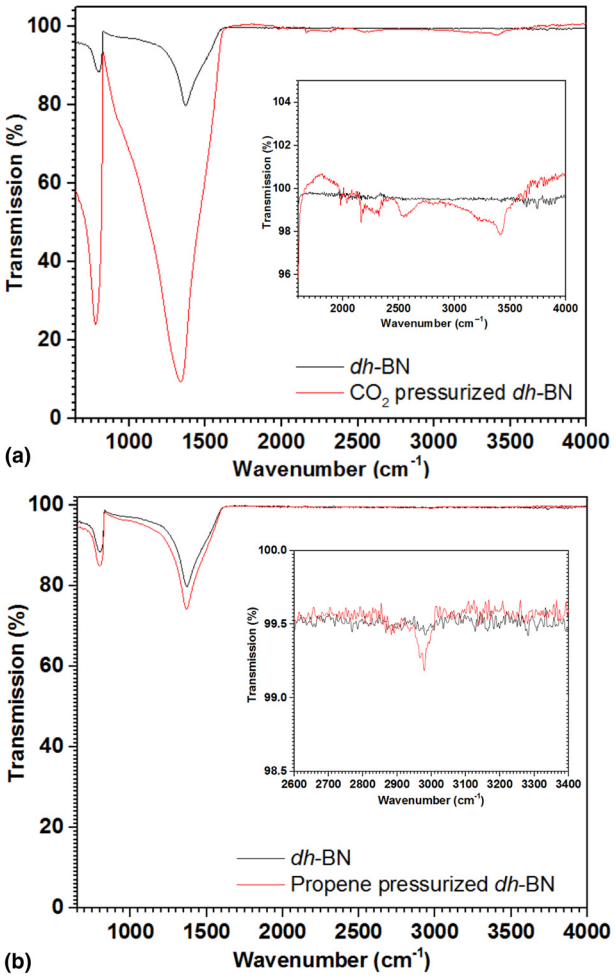


Figure 5. FTIR spectra of ball-milled BN powders before (black) and after pressurization for 48 h under 40 PSI (red) in CO_2 (a) and in propene (b). Insets provide details of the IR bands in the 1500–4000 cm^{-1} region.

products of a reaction on the flakes. In addition, the C-H asymmetric stretching mode ~2980 cm^{-1},[36] in agreement with the presence of propene or propane, was observed in the propene-pressurized dh-BN powder [inset in Fig. 5(b)]. Neither band was present in the *dh*-BN spectrum acquired prior to placing the powder in the pressure cell. No signal could be detected on the heat treated powders, likely due to the small concentration of molecules.

Conclusion

Ball milling and heat treatment lead to the formation of different defects in *h*-BN flakes. Particularly the microstructure and surface area of the flakes can be controlled by varying the duration of the treatment and the composition of milling media. For heat treatment, varying the temperature and duration of treatment was also found to affect the properties of the flakes. Raman and FTIR spectroscopy can be used to monitor defect creation, strain induction or oxidation of the sites created

https://doi.org/10.1557/mrc.2018.113 Published online by Cambridge University Press

depending on the conditions of the treatments. For instance, signals from impurities (~925 cm^{-1}) could be differentiated from oxidation taking place in the flakes resulting in the stronger band at 3200 cm^{-1}. In addition to deepening the fundamental understanding of processing–structure–property relationship of *h*-BN, our study has practical implications for the induction of catalytic sites in *h*-BN for reaction activation. Initial demonstration of the reactivity of *dh*-BN shows that the reaction is greatly treatment dependent. The detailed of catalytic activity, including the mechanism and the kinetics of the processes taking place after defect induction, will be the subject of future studies.

Supplementary material

The supplementary material for this article can be found at https://doi.org/10.1557/mrc.2018.113.

Acknowledgments

The authors would like to thank Saint-Gobain Ceramic Materials for the generous donation of hexagonal boron nitride powders used in this study. We acknowledge the NSF support for CHE-1465105 entitled "SusChEM: Defect-laden 2D Catalysts for Carbon Sequestration and Safer Hydrogenation".

References

1. V. Solozhenko, A. Lazarenko, J.-P. Petitet, and A. Kanaev: Bandgap energy of graphite-like hexagonal boron nitride. *J. Phys. Chem. Solids* **62**, 1331 (2001).
2. J. Tian, J. Lin, M. Xu, S. Wan, J. Lin, and Y. Wang: Hexagonal boron nitride catalyst in a fixed-bed reactor for exothermic propane oxidation dehydrogenation. *Chem. Eng. Sci.* **186**, 142 (2018).
3. D.J. Nash, D.T. Restrepo, N.S. Parra, K.E. Giesler, R.A. Penabade, M. Aminpour, D. Le, Z. Li, O.K. Farha, and J.K. Harper: Heterogeneous metal-free hydrogenation over defect-laden hexagonal boron nitride. *ACS Omega* **1**, 1343 (2016).
4. L. Li, Y. Liu, X. Yang, X. Yu, Y. Fang, Q. Li, P. Jin, and C. Tang: Ambient carbon dioxide capture using boron-rich porous boron nitride: a theoretical study. *ACS Appl. Mater. Interfaces* **9**, 15399 (2017).
5. J.T. Grant, C.A. Carrero, F. Goeltl, J. Venegas, P. Mueller, S.P. Burt, S. E. Specht, W.P. McDermott, A. Chieregato, and I. Hermans: Selective oxidative dehydrogenation of propane to propene using boron nitride catalysts. *Science* **354**, 1570 (2016).
6. J.M. Venegas, J.T. Grant, W.P. McDermott, S.P. Burt, J. Micka, C. A. Carrero, and I. Hermans: Selective oxidation of n-butane and isobutane catalyzed by boron nitride. *ChemCatChem.* **9**, 2118 (2017).
7. J.T. Grant, W.P. McDermott, J.M. Venegas, S.P. Burt, J. Micka, S. P. Phivilay, C.A. Carrero, and I. Hermans: Boron and boron-containing catalysts for the oxidative dehydrogenation of propane. *ChemCatChem.* **9**, 3623 (2017).
8. V. Fomichev, A. Rudnev, and S. Nemnonov: X-Ray emission bands of transition metals of the first long period. *Soviet Physics Solid State* **13**, 1031 (1971).
9. L. Carpenter, and P. Kirby: The electrical resistivity of boron nitride over the temperature range 700 degrees C to 1400 degrees C. *J. Phys. D: Appl. Phys.* **15**, 1143 (1982).
10. D. Akinwande, N. Petrone, and J. Hone: Two-dimensional flexible nanoelectronics. *Nat. Commun.* **5**, 5678 (2014).
11. K. Watanabe, T. Taniguchi, T. Niiyama, K. Miya, and M. Taniguchi: Far-ultraviolet plane-emission handheld device based on hexagonal boron nitride. *Nat. Photonics* **3**, 591 (2009).
12. L. Zhong, R.C. Bruno, K. Ethan, L. Ruitao, R. Rahul, T. Humberto, A. P. Marcos, and T. Mauricio: Defect engineering of two-dimensional transition metal dichalcogenides. *2D Materials* **3**, 022002 (2016).
13. Q. Peng, J. Crean, A.K. Dearden, C. Huang, X. Wen, S. Bordas and S. De: Defect Engineering of 2D monoatomic-layer materials. *Mod. Phys. Lett. B* **27**, 1330017 (2013).
14. A. Sajid, J.R. Reimers, and M.J. Ford: Defect states in hexagonal boron nitride: assignments of observed properties and prediction of properties relevant to quantum computation. *Phys Rev B.* **97**, 064101 (2018).
15. N.L. McDougall, J.G. Partridge, R.J. Nicholls, S.P. Russo, and D. G. McCulloch: Influence of point defects on the near edge structure of hexagonal boron nitride. *Phys Rev B.* **96**, 144106 (2017).
16. H. Henck, D. Pierucci, Z.B. Aziza, M.G. Silly, B. Gil, F. Sirotti, G. Cassabois, and A. Ouerghi: Stacking fault and defects in single domain multilayered hexagonal boron nitride. *Appl. Phys. Lett.* **110**, 023101 (2017).
17. B. Berzina, V. Korsaks, L. Trinkler, A. Sarakovskis, J. Grube, and S. Bellucci: Defect-induced blue luminescence of hexagonal boron nitride. *Diamond Relat. Mater.* **68**, 131 (2016).
18. J. Kroes, A. Fasolino, and M. Katsnelson: Energetics, barriers and vibrational spectra of partially and fully hydrogenated hexagonal boron nitride. *Phys. Chem. Chem. Phys.* **18**, 19359 (2016).
19. S. Immohr, M. Felderhoff, C. Weidenthaler, and F. Schüth: An orders-of-magnitude increase in the rate of the solid-catalyzed CO oxidation by in situ ball milling. *Angew. Chem., Int. Ed.* **52**, 12688 (2013).
20. B. Rodriguez, A. Bruckmann, T. Rantanen, and C. Bolm: Solvent-free carbon-carbon bond formations in ball mills. *Adv. Synth. Catal.* **349**, 2213 (2007).
21. R. Eckert, M. Felderhoff, and F. Schüth: Preferential carbon monoxide oxidation over copper-based catalysts under in situ ball milling. *Angew. Chem.* **129**, 2485 (2017).
22. V. Molchanov, R. Byanov, and V. Goidin: Use of mechanochemical methods in preparation of supported catalysts. *Kinet. Catal.* **39**, 434 (1998).
23. V. Zazhigalov, J. Haber, J. Stoch, L. Bogutskaya, and I. Bacherikova: Mechanochemistry as activation method of the VPO catalysts for n-butane partial oxidation. *Appl. Catal., A* **135**, 155 (1996).
24. J. Ghosh, S. Mazumdar, M. Das, S. Ghatak, and A. Basu: Microstructural characterization of amorphous and nanocrystalline boron nitride prepared by high-energy ball milling. *Mater. Res. Bull.* **43**, 1023 (2008).
25. J. Huang, X. Jia, H. Yasuda, and H. Mori: Stacking disordering in hexagonal BN induced by shearing under ball milling. *Philos. Mag. Lett.* **79**, 217 (1999).
26. D. Graf, F. Molitor, K. Ensslin, C. Stampfer, A. Jungen, C. Hierold, and L. Wirtz: Spatially resolved Raman spectroscopy of single-and few-layer graphene. *Nano Lett.* **7**, 238 (2007).
27. S. Mignuzzi, A.J. Pollard, N. Bonini, B. Brennan, I.S. Gilmore, M. A. Pimenta, D. Richards, and D. Roy: Effect of disorder on Raman scattering of single-layer MoS2. *Phys Rev B.* **91**, 195411 (2015).
28. N. Kang, H.P. Paudel, M.N. Leuenberger, L. Tetard, and S.I. Khondaker: Photoluminescence quenching in single-layer MoS2 via oxygen plasma treatment. *J. Phys. Chem. C.* **118**, 21258 (2014).
29. L.H. Li and Y. Chen: Atomically thin boron nitride: unique properties and applications. *Adv. Funct. Mater.* **26**, 2594 (2016).
30. Y. Kobayashi, K.-I. Fukui, T. Enoki, K. Kusakabe, and Y. Kaburagi: Observation of zigzag and armchair edges of graphite using scanning tunneling microscopy and spectroscopy. *Phys Rev B.* **71**, 193406 (2005).
31. A. Hashimoto, K. Suenaga, A. Gloter, K. Urita, and S. Iijima: Direct evidence for atomic defects in graphene layers. *Nature* **430**, 870 (2004).
32. S. Torii, K. Jimura, S. Hayashi, R. Kikuchi, and A. Takagaki: Utilization of hexagonal boron nitride as a solid acid–base bifunctional catalyst. *J. Catal.* **355**, 176 (2017).
33. B. Fakrach, A. Rahmani, H. Chadli, K. Sbai, M. Bentaleb, J.-L. Bantignies, and J.-L. Sauvajol: Infrared spectrum of single-walled boron nitride nanotubes. *Phys Rev B.* **85**, 115437 (2012).
34. E. Aradi, S. Naidoo, D. Billing, D. Wamwangi, I. Motochi, and T.E. Derry: Ion beam modification of the structure and properties of hexagonal boron nitride: an infrared and x-ray diffraction study. *Nucl. Instrum. Methods Phys. Res., Sect. B* **331**, 140 (2014).
35. J.S.M. Nithya and A. Pandurangan: Efficient mixed metal oxide routed synthesis of boron nitride nanotubes. *RSC Adv.* **4**, 26697 (2014).

https://doi.org/10.1557/mrc.2018.113 Published online by Cambridge University Press

36. M.I. Baraton, T. Merle, P. Quintard, and V. Lorenzelli: Surface activity of a boron nitride powder: a vibrational study. *Langmuir* **9**, 1486 (1993).
37. J. Li, X. Xiao, X. Xu, J. Lin, Y. Huang, Y. Xue, P. Jin, J. Zou, and C. Tang: Activated boron nitride as an effective adsorbent for metal ions and organic pollutants. *Sci. Rep.* **3**, 3208 (2013).
38. C. Tang, Y. Bando, Y. Huang, C. Zhi, and D. Golberg: Synthetic routes and formation mechanisms of spherical boron nitride nanoparticles. *Adv. Funct. Mater.* **18**, 3653 (2008).
39. L.H. Li, J. Cervenka, K. Watanabe, T. Taniguchi, and Y. Chen: Strong oxidation resistance of atomically thin boron nitride nanosheets. *ACS Nano* **8**, 1457 (2014).
40. Y. Liao, K. Tu, X. Han, L. Hu, J.W. Connell, Z. Chen, and Y. Lin: Oxidative etching of hexagonal boron nitride toward nanosheets with defined edges and holes. *Sci. Rep.* **5**, 14510 (2015).
41. Q. Yang, J. Sha, L. Wang, Y. Zou, J. Niu, C. Cui, and D. Yang: Crystalline boron oxide nanowires on silicon substrate. *Physica E* **27**, 319 (2005).

https://doi.org/10.1557/mrc.2018.113 Published online by Cambridge University Press